Chemical Research in Toxicology

pubs.acs.org/crt

Article

Cytocompatibility of $Ti_3C_2T_x$ MXene with Red Blood Cells and Human Umbilical Vein Endothelial Cells and the Underlying Mechanisms

Jian Huang,[#] Juan Su,[#] Zhenyu Hou, Jing Li, Zheming Li, Zhu Zhu, Shengtang Liu, Zaixing Yang, Xiuhua Yin,* and Gang Yu*

Cite This: *Chem. Res. Toxicol.* 2023, 36, 347−359

Read Online

ACCESS | Metrics & More | Article Recommendations | Supporting Information

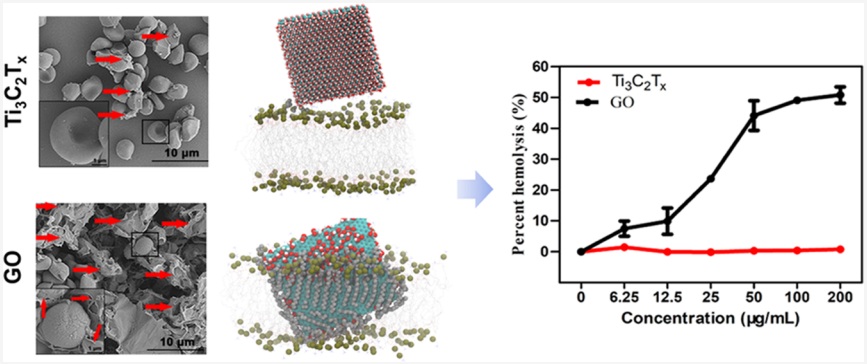

ABSTRACT: Two-dimensional (2D) nanomaterials have been widely used in biomedical applications because of their biocompatibility. Considering the high risk of exposure of the circulatory system to $Ti_3C_2T_x$, we studied the cytocompatibility of $Ti_3C_2T_x$ MXene with red blood cells (RBCs) and human umbilical vein endothelial cells (HUVECs) and showed that $Ti_3C_2T_x$ had excellent compatibility with the two cell lines. $Ti_3C_2T_x$ at a concentration as high as 200 μg/mL caused a negligible percent hemolysis of 0.8%. By contrast, at the same treatment concentration, graphene oxide (GO) caused a high percent hemolysis of 50.8%. Scanning electron microscopy revealed that RBC structures remained intact in the $Ti_3C_2T_x$ treatment group, whereas those in the GO group completely deformed, sunk, and shrunk, which resulted in the release of cell contents. This difference can be largely ascribed to the distinct surficial properties of the two nanosheets. In specific, the fully covered surface-terminating −O and −OH groups leading to $Ti_3C_2T_x$ had a very hydrophilic surface, thereby hindering its penetration into the highly hydrophobic interior of the cell membrane. However, the strong direct van der Waals attractions coordinated with hydrophobic interactions between the unoxidized regions of GO and the lipid hydrophobic tails can still damage the integrity of the cell membranes. In addition, the sharp and keen-edged corners of GO may also facilitate its relatively strong cell membrane damage effects than $Ti_3C_2T_x$. Thus, the excellent cell membrane compatibility of $Ti_3C_2T_x$ nanosheets and their ultraweak capacity to provoke excessive ROS generation endowed them with much better compatibility with HUVECs than GO nanosheets. These results indicate that $Ti_3C_2T_x$ has much better cytocompatibility than GO and provide a valuable reference for the future biomedical applications of $Ti_3C_2T_x$.

INTRODUCTION

In 2011, the discovery of MXenes, a family of two-dimensional (2D) nanomaterials, sparked a research boom because of their intriguing physical and chemical properties.[1] MXenes are composed of external transition-metal oxides/hydroxides and internal transition-metal carbides, resulting in their good electrical conductivity, high photothermal conversion efficiency, and fluorescence imaging properties. Given these characteristics and their high specific surface areas, MXenes have been extensively studied in the fields of energy,[2−4] storage systems,[5−7] electronic devices,[8−11] electromagnetic shielding,[12−15] and water desalination/purification membranes.[16−19] In addition, MXenes have been extensively studied for their biomedical applications,[20] including biosensing,[21−27] antibacterial activity,[28−32] drug delivery,[33−35] tumor photothermal therapy,[36−40] artificial bio-synapse,[41,42] and bioimaging.[43−45]

One of the most studied MXenes is $Ti_3C_2T_x$ (T stands for surface termination and represents functional groups such as −O, −OH, and −F). For instance, Yan et al.[41] have shown that

Received: May 10, 2022
Published: February 15, 2023

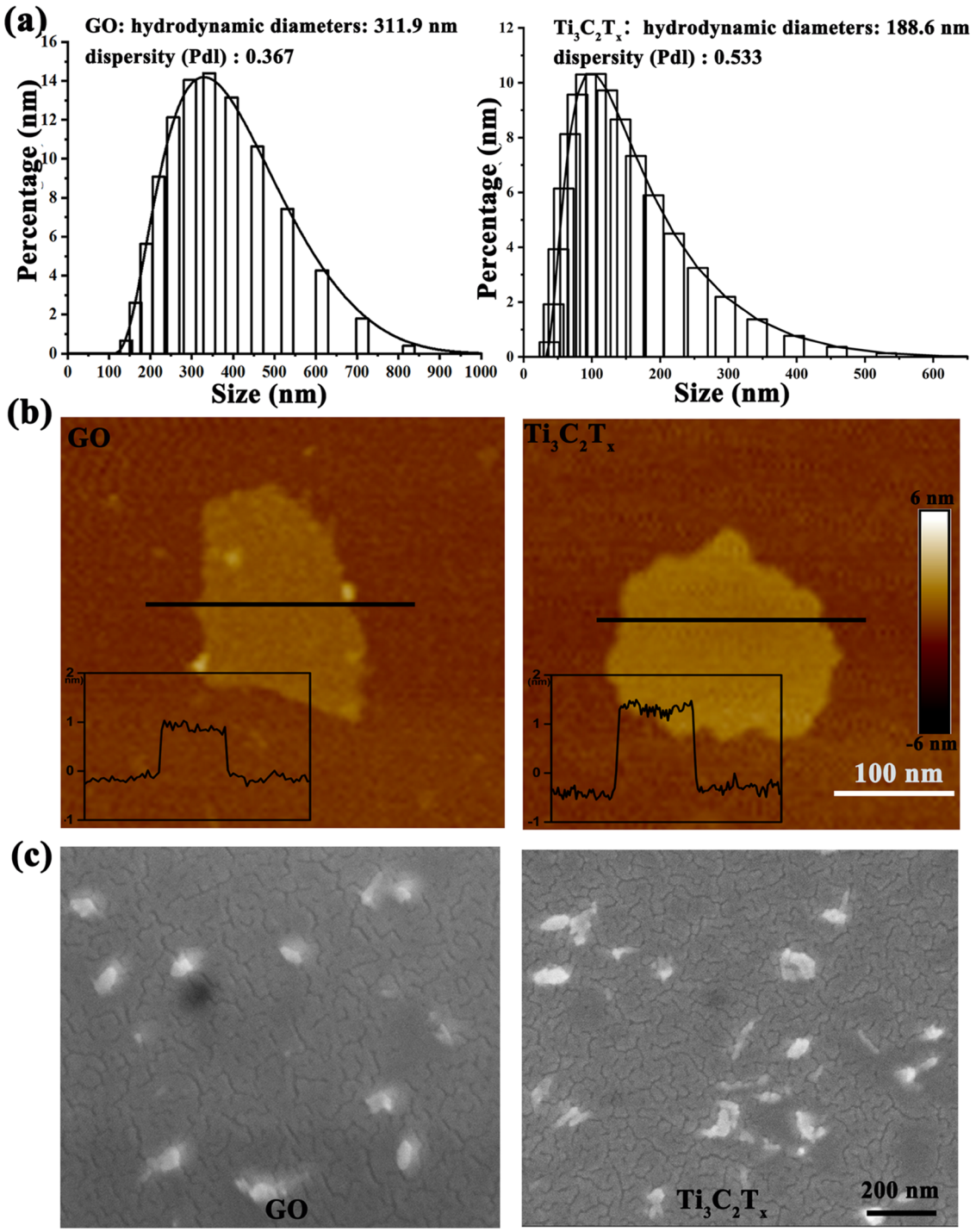

Figure 1. Characterization of $Ti_3C_2T_x$ and GO nanosheets. (a) DLS intensity distributions. (b) AFM images; the inset shows the height maps of the cross sections at the black lines. (c) SEM images.

$Ti_3C_2T_x$ MXene microelectrodes perform well in recording nerve activity. Zhang et al[46] have reported that MXene-doped fiber belts can be used as a near-infrared (NIR)-responsive vitamin E carrier to promote wound healing *in vivo*. Mahmoud et al.[29] have demonstrated that $Ti_3C_2T_x$ has good antibacterial properties and is a potential antibacterial agent. Ahamed et al.[47] have illustrated the antifungal function of $Ti_3C_2T_x$. In addition, $Ti_3C_2T_x$ and other MXene materials have been applied in the photothermal therapy of tumors owing to their high photothermal conversion efficiency.[39] Given their strong optical absorption properties and excellent photothermal conversion efficiency under a wide spectral region (e.g., ranging from ultraviolet to visible light to NIR), they show high potential in treating diseases in deep tissues.[39,40,48−54] Predictably, $Ti_3C_2T_x$ and other MXene materials may offer great promise in biomedicine.

However, research on the cytocompatibility of $Ti_3C_2T_x$ is still insufficient because of the high complexity of the response of various cell lines to the stimulus of $Ti_3C_2T_x$.[55−57] For instance, Ti_3C_2 nanosheets were reported to have a relatively high cytocompatibility with HUVECs.[58] Specifically, only at a very high treatment concentration (500 μg/mL), they could

https://doi.org/10.1021/acs.chemrestox.2c00154
Chem. Res. Toxicol. 2023, 36, 347−359

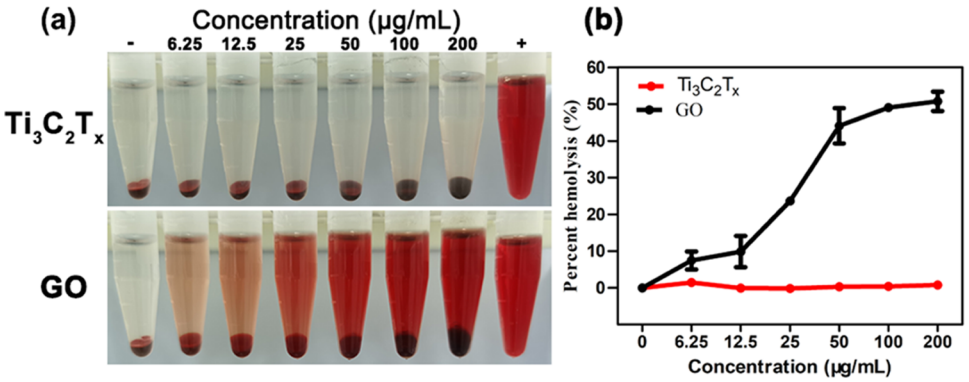

Figure 2. Hemolytic activity of $Ti_3C_2T_x$ and GO nanosheets. (a) Hemolytic properties of the two nanosheets were assessed by the colors of cell supernatants when RBCs were treated with $Ti_3C_2T_x$ and GO nanosheets at different concentrations (6.25−200 μg/mL). The (+) and (−) signs indicate the positive and negative controls, respectively. (b) The percent hemolysis of each group of cells is shown in panel (a). The cells were treated for 3 h.

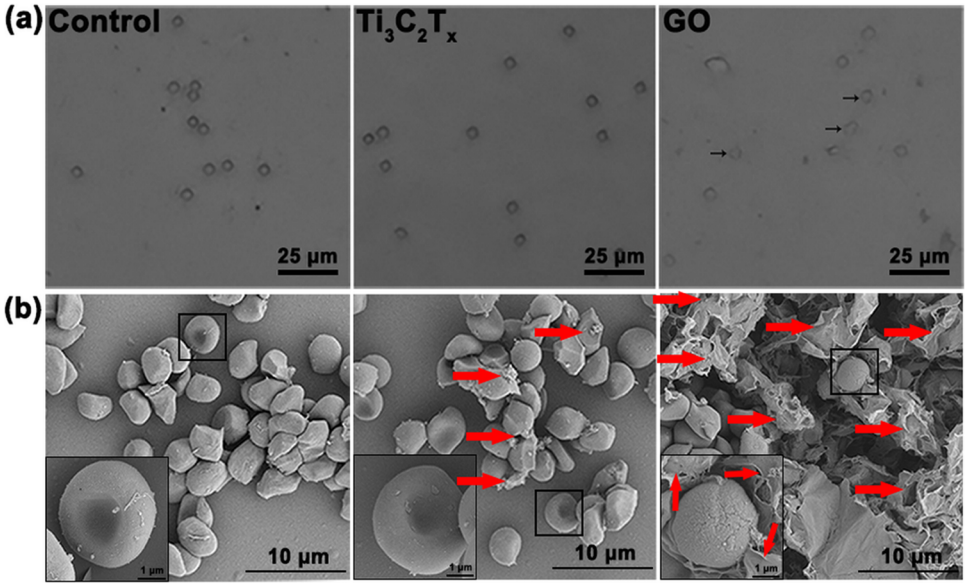

Figure 3. Observation of RBC morphology. The RBC morphology was observed via (a) light microscopy and (b) SEM.

induce significant changes in the energy metabolism of HUVECs, which was attributed to the injury of mitochondria. However, Ti_3C_2 quantum dots showed higher cytotoxicity with HUVECs.[59] They can trigger serving cytotoxicity at a much lower treatment concentration (100 μg/mL) via disruption of autophagy. Interestingly, $Ti_3C_2T_x$ nanosheets exhibited higher toxic effects on cancerous cells (A549, A375, MCF7, and HeLa) over normal cells (MRC-5, HaCaT, IMR90, MCF10A, and human fibroblasts) due to their relative stronger capability to provoke a higher intracellular ROS level and adhesion to cell membranes of cancer cells.[47,60,61] In addition, $Ti_3C_2T_x$ nanosheets demonstrated high cytotoxicity with primary neural stem cells (NSCs) and NSC-derived differentiated cells.[62] On treatment at 25 μg/mL, they can elicit significant cytotoxicity via the destruction of cell membranes. $Ti_3C_2T_x$ nanosheets also had high toxicity to human mesenchymal stem cells, when the treatment concentration was larger than 50 μg/mL.[63] Thus, these uncertainties constitute some essential biosecurity concerns.[56,64]

Considering the fact that the circulatory system may have a high risk of exposure to $Ti_3C_2T_x$ in many biomedical applications, red blood cells (RBCs) are the most abundant blood cells in the circulatory system and human umbilical vein endothelial cells (HUVECs) are the dominant component of the inner lining of major blood vessels. Thus, RBCs and HUVECs are likely to be the first living components encountered by nanomedicine injected intravenously into the human body. Accordingly, we studied the compatibility of $Ti_3C_2T_x$ with RBCs and HUVECs and elucidated the underlying mechanisms. Graphene oxide (GO) was set as the control since it is a star 2D nanomaterial, which has been most extensively used in bioapplications. Our results showed that $Ti_3C_2T_x$ was more compatible than GO with these two types of cells, especially RBCs. The better cytocompatibility of $Ti_3C_2T_x$ than GO was mainly due to its better compatibility with the cell membranes. Our findings provide important references for possible safe biomedical applications of $Ti_3C_2T_x$ in the future.

RESULTS AND DISCUSSION

The structural properties of $Ti_3C_2T_x$ nanosheets were characterized using dynamic light scattering (DLS), atomic force microscopy (AFM), X-ray diffraction (XRD), Raman spectroscopy, and X-ray photoelectron spectroscopy (XPS)

https://doi.org/10.1021/acs.chemrestox.2c00154
Chem. Res. Toxicol. 2023, 36, 347−359

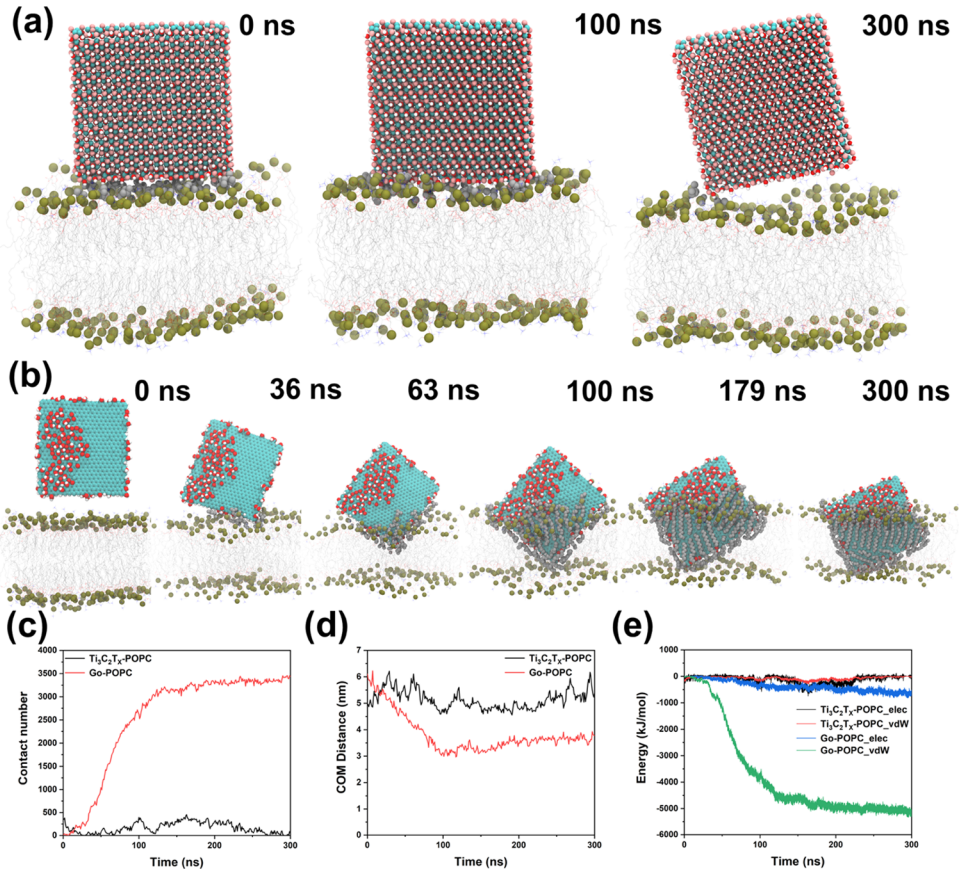

Figure 4. (a, b) Representative trajectories of a $Ti_3C_2T_x$/GO nanosheet on a POPC membrane. Silver lines show phospholipids in POPC membranes. P, Ti, C, O, and H atoms are shown in lime green, pink, cyan, O red, and white, respectively. The time evolution of (c) the atom contact number and (d) the center-of-mass (COM) distance between $Ti_3C_2T_x$/GO and the membrane. (e) The electrostatic (elec) and vdW interaction energies between $Ti_3C_2T_x$/GO and the membrane.

(Figures 1 and S1−S3). GO nanosheets, typical 2D nanomaterials widely studied in the biomedical field, were set as the control. Further characterization details about GO nanosheets are provided in our previous literature.[65] Water-dispersed GO and $Ti_3C_2T_x$ nanosheets displayed average hydrodynamic diameters of 311.9 (Pdl: 0.367) and 188.6 nm (Pdl: 0.533) by DLS; and, their ζ-potentials were 0.04 and −0.01, respectively (Figure 1a and Table S1). AFM imaging (Figure 1b) revealed that the thicknesses of $Ti_3C_2T_x$ and GO nanosheets were ∼1.3 and 0.9 nm, respectively. However, GO nanosheets had much more keen-edged corners than $Ti_3C_2T_x$ (Figure S4). SEM images (Figure 1c) exhibited well-distributed $Ti_3C_2T_x$/GO nanosheets, where the morphology of the flakes was observed. These data indicate that these two types of nanosheets had several similar morphological characteristics, such as lateral size, thickness, roughness, and uneven shape, but with varying sharp degrees of corners. XPS suggested that the surface-terminating groups of $Ti_3C_2T_x$ nanosheets should be mainly the −O and −OH groups (Figure S3). However, the surface of GO nanosheets contains C−O−C, −OH, −COOH, and C═O groups.[65]

RBCs are the most abundant blood cells in the human body and are the first tissue encountered by nanomedicine injected intravenously. Studying the biocompatibility of $Ti_3C_2T_x$ and GO nanosheets with RBCs, especially their impact on the integrity of RBC membranes, is important to evaluate the biomedical application of the materials. We conducted *in vitro* hemolysis, a method commonly performed in previous studies.[66−68] As shown in Figure 2a, the supernatant of the RBCs coincubated with $Ti_3C_2T_x$ was clear and transparent, whereas that of the RBCs coincubated with GO changed color from light red to dark red as the GO concentration was increased. As shown in Figure 2b, the percent hemolysis increased rapidly as the GO concentration was increased. The percent hemolysis of GO at 200 μg/mL concentration reached 50.8%, whereas that of $Ti_3C_2T_x$ was only 0.8%. These results confirm the excellent cytocompatibility of $Ti_3C_2T_x$ with RBCs.

The results of the above hemolysis assay were verified using light microscopy and scanning electron microscopy (SEM). Under light microscopy (Figure 3a), the morphology of the RBCs incubated with $Ti_3C_2T_x$ nanosheets was similar to that of the RBCs in the control group. However, the morphology of the RBCs coincubated with GO was clearly different, showing a flattened or irregular shape (as indicated by black arrows in Figure 3a). In addition, SEM imaging (Figure 3b) confirmed the findings of light microscopy—that the RBCs coincubated with $Ti_3C_2T_x$ nanosheets maintained their typical biconcave disc shape (similar to the control group), but the edges of the RBCs incubated with GO nanosheets were disrupted and had severely deformed shapes. Microscopic observation results showed that $Ti_3C_2T_x$ nanosheets did not damage the RBC membranes and had good cell membrane compatibility, which can also explains their good RBC compatibility.

Then, we used all-atomic molecular dynamics (MD) simulations to further unravel the interface behavior and the underlying mechanisms between a $Ti_3C_2T_x$/GO nanosheet

https://doi.org/10.1021/acs.chemrestox.2c00154
Chem. Res. Toxicol. 2023, 36, 347−359

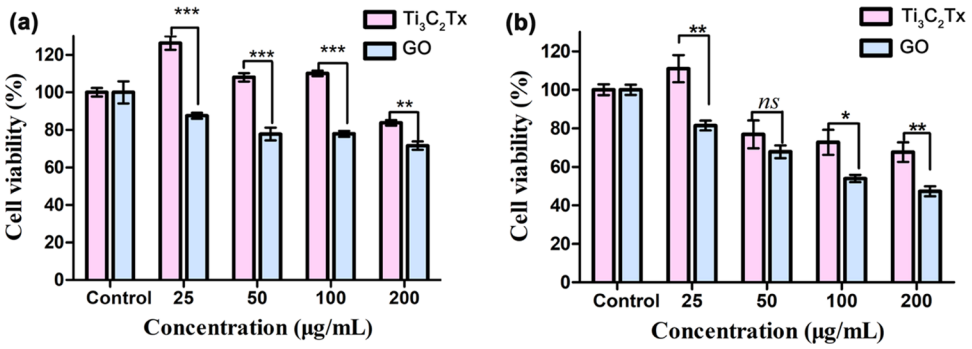

Figure 5. HUVEC viability after $Ti_3C_2T_x$ and GO treatments analyzed by the CCK-8 assay. HUVEC survival rates after incubation with different concentrations of $Ti_3C_2T_x$ and GO for (a) 24 h and (b) 48 h. Data are presented as mean ± s.d., $n = 6$ per group. *$p < 0.05$; **$p < 0.01$; and ***$p < 0.001$ between groups by t-test.

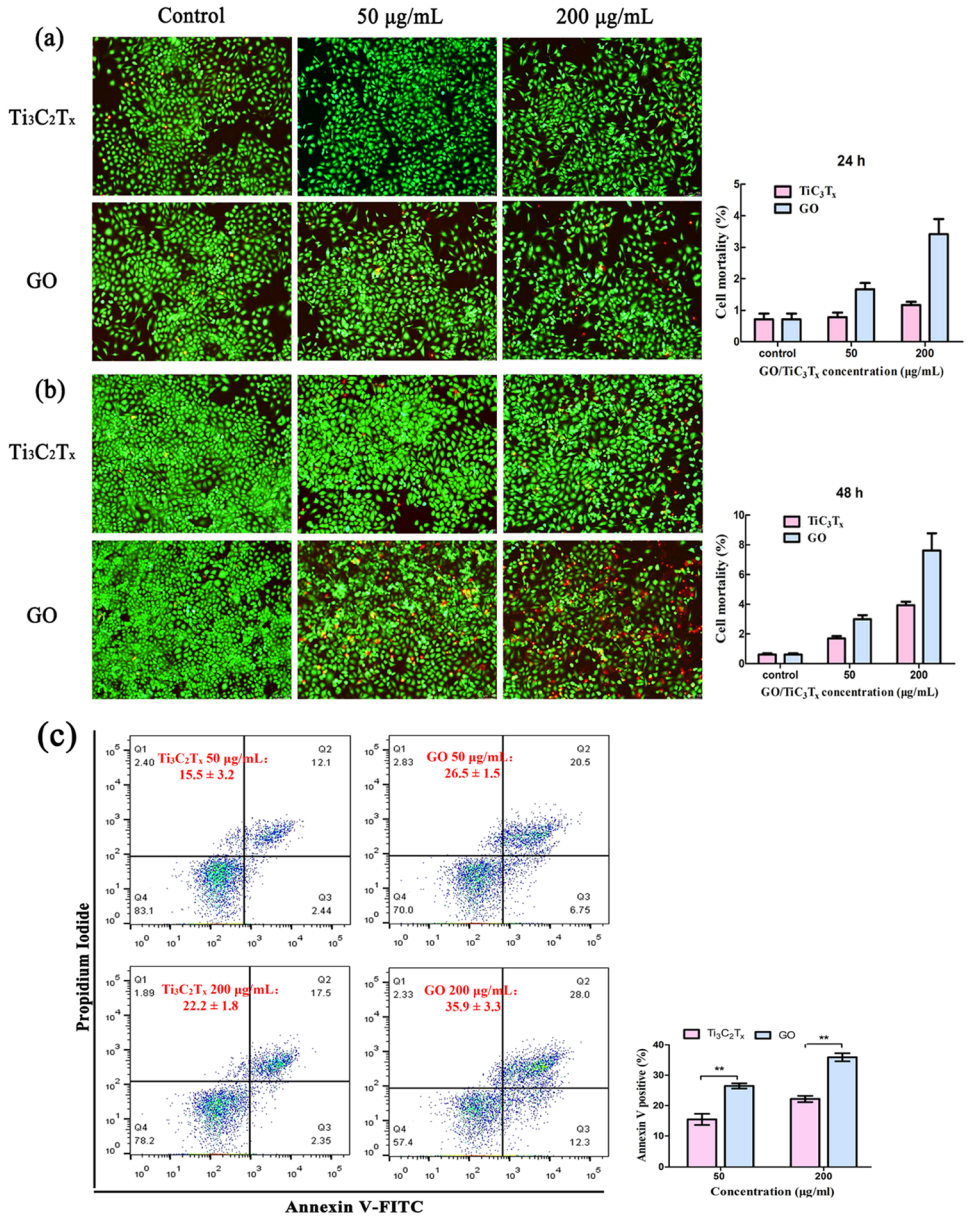

Figure 6. HUVEC viabilities after $Ti_3C_2T_x$ and GO nanosheet treatments analyzed by the LIVE/DEAD kit for (a) 24 h and (b) 48 h. (c) Cellular apoptosis was measured by annexin V staining and flow cytometry. Data are represented as the mean ± s.d., $n = 3$. Scale bar = 100 μm.

and the cell membrane. Figure 4a,b shows the trajectories of a $Ti_3C_2T_x$/GO nanosheet interacting with the POPC model membrane. Clearly, within the simulation timescale of 300 ns, $Ti_3C_2T_x$ cannot insert into the membrane and destructively

https://doi.org/10.1021/acs.chemrestox.2c00154
Chem. Res. Toxicol. 2023, 36, 347−359

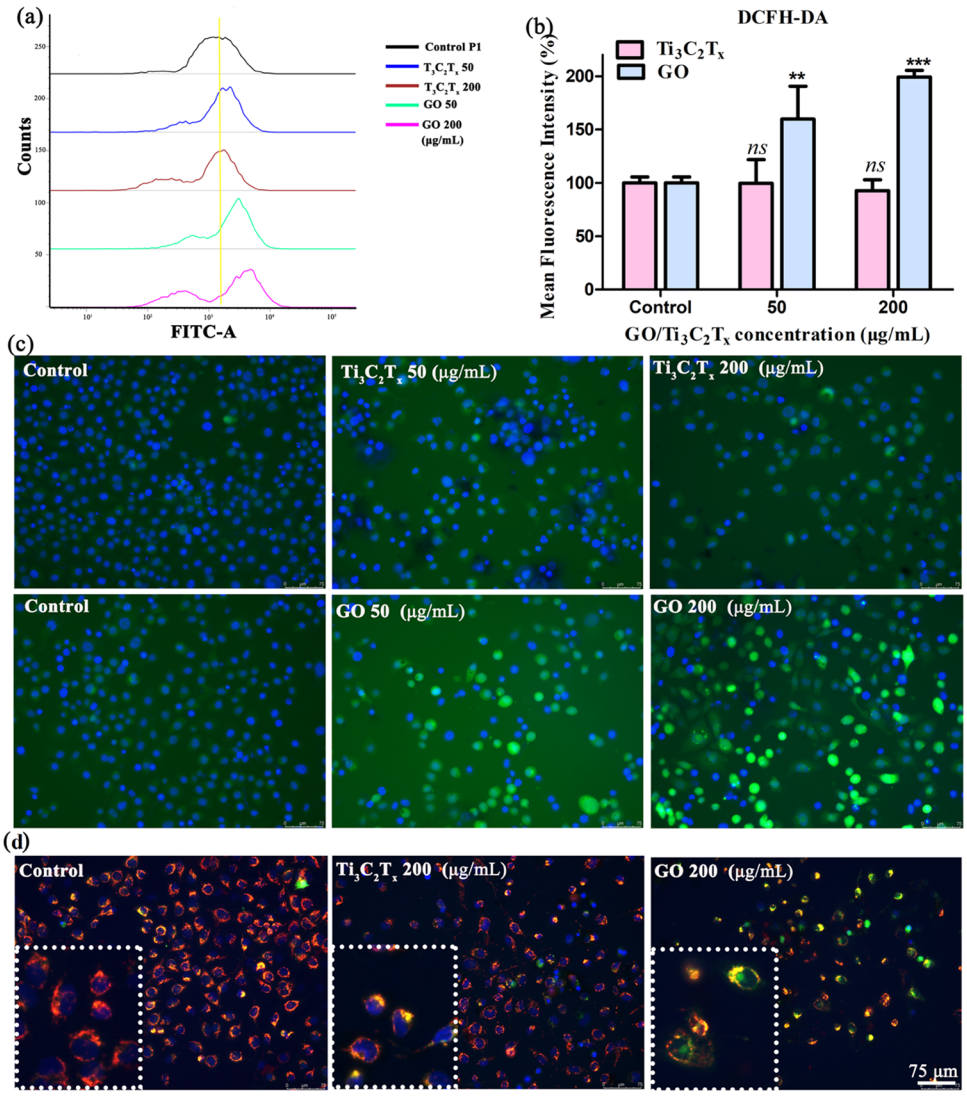

Figure 7. ROS levels in HUVECs after 48 h incubation with $Ti_3C_2T_x$/GO nanosheets at 50 and 200 μg/mL. (a, b) The ROS level was measured by flow cytometry. Data are represented as mean ± s.d., $n = 3$, $^{**}p < 0.01$, $^{***}p < 0.001$ vs the control group by t-test. (c) Representative micrographs of HUVECs for the detection of intracellular ROS. Blue: cell nuclei stained by Hoechst 33342 dye; green: DCF fluorescence generated from the oxidization of nonfluorescent DCFH by ROS. (d) Fluorescence imaging of JC-1 staining after $Ti_3C_2T_x$/GO nanosheet treatment. Blue: cell nuclei stained by Hoechst 33342 dye; red and green: mitochondrial membrane potential as determined by JC-1 staining. If MMP depolarizes, JC-1 becomes a monomer (green); if it polarizes, it becomes a polymer (red). Scar bar: 100 μm.

extract phospholipid molecules out of the membrane. This can be confirmed by the time evolution of the atom contact number and the center-of-mass (COM) distance between $Ti_3C_2T_x$ and the membrane because the two indexes only had a very mild change over time. During the process, both the electrostatic and van der Waals (vdW) interaction energies decreased weakly, while the former declined apparently more than the latter. In contrast, GO nanosheet can quickly penetrate into the membrane and extract phospholipid molecules from the membrane. At the early stage, the shape corner on the unoxidized region (sp^2 domain) first penetrated into the membrane; then, more sp^2 domain region inserted into the membrane and was accompanied by the lipid extraction from the membrane. At the end of the simulation, the sp^2 domain region was fully covered with lipid molecules; however, only the partially oxidized region was covered with lipid molecules. The interaction energy analysis demonstrates that vdW interactions had a remarkable contribution to the behaviors of the GO nanosheet on the membrane; while, the electrostatic interactions had a relatively weaker contribution. The observed interacting behaviors of GO nanosheet with the membrane here are consistent with previous literature.[69−71] The distinct behavior of the two nanosheets on the surface of the membrane may partially arise from the difference in the surface physical and chemical properties of the two nanosheets.

The surface of $Ti_3C_2T_x$ is fully covered with the polar −O and −OH groups showing high hydrophilicity,[72] thereby hindering its penetration into the highly hydrophobic interior of the cell membrane. Although the surface of GO also contains C−O−C, −OH, −COOH, and C═O groups, a large area of unoxidized regions (sp^2 domain) remains as illustrated by the characterizations using ultra-high-resolution transmission electron microscopy in several previous literature studies.[73−75] Specifically, Gómez-Navarro et al.[73] reported that the unoxidized regions of GO can reach ∼60%. Therefore, the strong direct vdW attractions coordinated with hydrophobic

https://doi.org/10.1021/acs.chemrestox.2c00154
Chem. Res. Toxicol. 2023, 36, 347−359

interactions between those unoxidized regions with the lipid hydrophobic tails can still destroy the cell membrane.[69,76] In addition, the keen-edged corners of GO nanosheets should also facilitate their cell membrane damage effects, promoting hemolytic activity (Figure S4). The important role of these sharp corner sites in assisting GO nanosheets to penetrate cell membranes had been thoroughly illustrated previously by combining multiscale modeling and imaging experiments.[71]

We further studied the cytocompatibility of $Ti_3C_2T_x$ to HUVECs. To quantify the cytotoxicity of $Ti_3C_2T_x$ and GO nanosheets, we first used the cell counting kit-8 (CCK-8) assay to analyze the effects of the two nanomaterials on the cell viability of HUVECs (Figure 5). In general, the cell viability negatively correlated with the incubation time and treatment concentration of the two nanomaterials, but $Ti_3C_2T_x$ nanosheets showed much better cytocompatibility than GO under the same conditions. For instance, at the concentration of 200 μg/mL for 24 h, the cell viability was ~83.7% in the $Ti_3C_2T_x$ nanosheets treatment group and 71.6% in the GO nanosheet treatment group (Figure 5a,b). When the treatment concentration of two nanosheets was further increased even to 600 μg/mL, the viability for cells treated with $Ti_3C_2T_x$ nanosheets was still much higher than that treated with GO nanosheets (~62.5% vs ~25.6%) (Figure S5). In addition, as the treatment duration time was extended to 48 h, the cytotoxicities caused by $Ti_3C_2T_x$ and GO also both elevated; at 200 μg/mL, the viability of HUVECs decreased to ~67.7% under $Ti_3C_2T_x$ treatment and to ~47.2% under GO treatment. The cell viability performance of $Ti_3C_2T_x$ nanosheets toward HUVECs here was qualitatively consistent with the findings by Zhang et al.[58] All of these results pronounced that $Ti_3C_2T_x$ nanosheets had decent cytocompatibility with HUVECs under the conditions.

The mortality of HUVECs after treatment with $Ti_3C_2T_x$ and GO nanosheets was evaluated using the LIVE/DEAD kit to verify the above results. As shown in Figure 6, the appearance of the dead cells (red dots) increased with the incubation time and treatment concentration of the two types of nanosheets. Thus, the cell mortality caused by the two nanosheets was dependent on treatment duration and dose. Moreover, the density of detected red signals in the $Ti_3C_2T_x$ nanosheet treatment group was much milder than that in the $Ti_3C_2T_x$ nanosheet treatment group under the same conditions (Figure 6a,b). At the highest treatment concentration of 200 μg/mL, the percentage of dead cells in the $Ti_3C_2T_x$ group increased from ~1.2 to ~3.6% as the treatment time was prolonged from 24 to 48 h. By contrast, the value increased from ~3.9 to ~11.9% in the GO nanosheet treatment group (Figure 6a,b). In addition, the apoptosis results obtained from flow cytometry using annexin V/propidium iodide were consistent with LIVE/DEAD staining results. Results showed that GO nanosheets indeed induced more apoptosis events than $Ti_3C_2T_x$ nanosheets on HUVECs (Figure 6c). Therefore, these results collaborated that $Ti_3C_2T_x$ nanosheets had much lower cytotoxicity than GO nanosheets with HUVECs.

We then measured the cellular uptake of two nanosheets using the side scattered light (SSC) assay. At equal treatment concentrations, GO nanosheets had a higher cellular uptake rate than $Ti_3C_2T_x$ (Figure S6). SEM imaging results demonstrated more GO nanosheets adhering to the cell membrane surfaces (Figure S7). In addition, GO nanosheets exhibited a relatively strong capability of damaging the integrity of cell membranes. Next, the intracellular reactive oxygen species (ROS) levels were detected because of their importance in inducing cytotoxicity by many nanomaterials.[77,78] Excessive production of ROS can induce cell damage via various mechanisms, such as interacting with and destroying cellular proteins, DNA, and lipids or affecting normal cellular signaling pathways, the integrity of the mitochondrial inner membrane, and gene regulation. The present results showed that $Ti_3C_2T_x$ nanosheets show a very weak capacity to cause the generation of extra intracellular ROS as compared with the control group even when the treatment concentration was increased to 200 μg/mL (Figure 7a,b). By contrast, GO nanosheets indeed provoked the generation of high-level ROS (Figure 6a,b), which agreed very well with previous literature.[65,77,78] In specific, the intracellular ROS level induced by GO nanosheets was about 2-fold that induced by the control and $Ti_3C_2T_x$ nanosheets at a concentration of 200 μg/mL and duration of 48 h ($p < 0.01$; Figure 7b). These results were further validated by the fluorescence microscope observations (Figure 7c, top and middle panels).

We further probed the depolarization status of the mitochondrial membrane potential (MMP) because it is an important indicator for the early apoptosis induced by ROS or other factors. The mitochondrion is a vital organelle for energy production and an important target of cellular oxidative damage.[79] When the mitochondrial inner membrane is destroyed under some external stimuli (e.g., peroxide by ROS), depolarization and the outflow of proapoptotic factors from the mitochondrion occur.[80] As shown in Figure 7d, the mitochondria in the control and $Ti_3C_2T_x$ nanosheet treatment groups showed red fluorescence signals, suggesting a normal MMP status. Consequently, $Ti_3C_2T_x$ nanosheets only had a very limited capacity to stimulate ROS generation, which improved their cytocompatibility. By contrast, extensive green fluorescence signals were detected in the cells after treatment with GO for 48 h, which indicated that GO-provoked ROS severely disrupted the mitochondrial inner membranes, thus inducing MMP depolarization and, eventually, cell apoptosis. Moreover, we also performed an impurity analysis of GO nanosheets, and the results showed that few sulfate and manganese groups can be detected in the original GO suspension (Figure S8). However, before treating cells, the original GO suspension (13.3 mg/mL) must undergo ~66- to ~532-fold dilution to the concentration of 200 μg/mL to 25 μg/mL, resulting in these impurities also undergoing at least 66-fold dilution. That said, impurities should not be a critical reason for the cytotoxicity of GO here.

CONCLUSIONS

In this study, we investigated the cytocompatibility of 2D $Ti_3C_2T_x$ MXene with RBCs and HUVECs and showed that $Ti_3C_2T_x$ had excellent compatibility with RBCs. Even when the $Ti_3C_2T_x$ treatment concentration was as high as 200 μg/mL, the percentage of hemolysis caused by $Ti_3C_2T_x$ was still negligible (only 0.8%). By contrast, under the same treatment concentration, the percent hemolysis caused by GO reached 50.8%. The morphological observation indicated that $Ti_3C_2T_x$ had better compatibility with the cell membranes and had nearly no effect on the integrity of the cell membranes when compared with GO. By contrast, GO caused extremely severe deformation, depression, and shrinkage of the cell membranes, causing the release of cellular contents. In addition, $Ti_3C_2T_x$ had much better compatibility with HUVECs than GO.

https://doi.org/10.1021/acs.chemrestox.2c00154
Chem. Res. Toxicol. 2023, 36, 347−359

The excellent cell membrane compatibility of $Ti_3C_2T_x$ nanosheets over GO nanosheets can be largely attributed to their more hydrophilic surface. For instance, the dominating surface-terminating groups of $Ti_3C_2T_x$ nanosheets are −O and −OH groups, thus increasing their adsorption onto the surface of the cell membrane through electrostatic or hydrogen binding interactions with the polar head group of membrane lipids. By contrast, the strong direct van der Waals attractions coordinated with hydrophobic interactions between the unoxidized regions of GO nanosheets and the lipid hydrophobic tails disrupted the cell membranes. On the other hand, these sharp corners on GO nanosheets also strengthen their cell membrane damage effects. Therefore, the excellent cell membrane compatibility of $Ti_3C_2T_x$ nanosheets and their ultraweak capacity to provoke the generation of excessive ROS endowed them with much better compatibility with HUVECs than GO nanosheets. In addition, previous literature studies have experimentally and theoretically demonstrated that serum protein coatings can alleviate the cytotoxicity of GO by lowering its cell membrane penetration capability.[70,81] This also suggests that in the presence of serum proteins, $Ti_3C_2T_x$ may also be able to form protein corona, and thus, the cell membrane compatibility of $Ti_3C_2T_x$ may further be relieved.

It should be emphasized that *in vitro* compatibility assessments are usually an initial step to evaluate the toxic effects of nanomaterials. Though these cell-based assays suggest that $Ti_3C_2T_x$ nanosheets have decent compatibility toward RBCs and HUVECs, the much-complicated *in vivo* toxicity still needs to be thoroughly examined. Because there are several previous literature studies that have demonstrated that different cell lines show distinct tolerance to the treatment dose of $Ti_3C_2T_x$ nanosheets.[47,60−63] The biodistribution of $Ti_3C_2T_x$ nanosheets also needs to be clearly identified when they were administered into the body by different routes. In addition, $Ti_3C_2T_x$ nanosheets can be degraded to small species (e.g., titanium dioxide, carbon, and other small species) via oxidation reaction with oxidizing agents, when exposed to air, water, or organic solvents.[27,72,82−88] This suggests that the biotransformation of $Ti_3C_2T_x$ nanosheets in physiological environments and its potential risk to the body also should be considered. On the whole, our findings provide an early glimpse into the cytocompatibility of $Ti_3C_2T_x$ MXene with RBCs and HUVECs, offering some useful references for the safe use of this material in biomedical applications in future.

MATERIALS AND METHODS

Materials and Characterizations. $Ti_3C_2T_x$ nanosheets were obtained from Nanjing MKNANO Tec Co., Ltd. (Nanjing, China). GO nanosheets were obtained from Timenano (characterization details are provided in our previous literature[65]). HUVECs were purchased from American Type Culture Collection (ATCC). Dulbecco's modified Eagle's medium (DMEM; cat#11965092), penicillin/streptomycin solution (P/S; cat#15140122), L-glutamine (cat#25030149), nonessential amino acids (cat#11140050), and 0.25% trypsin−EDTA solution (cat#25200056) were obtained from Gibco, Thermo Fischer Scientific (CA). Cell counting kit-8 (CCK-8, cat#ck04) was purchased from Dojindo Molecular Technologies Inc. (Kumamoto, Japan). Live/dead kits (cat#l3224) were from Life Technologies Corporation (Carlsbad, CA). Dulbecco's phosphate-buffered saline (PBS; cat#c0021a), fluorescent dye 2′,7′-dichlorofluorescin diacetate (DCFH-DA, cat#S0033M), and JC-1 kit (cat#C2006) were purchased from Beyotime Biotechnology (Shanghai, Chian). Calcein-AM and ethidium homodimer-1 (LIVE/DEAD kit, cat#l3224) were purchased from Invitrogen. Annexin V apoptosis detection kit (cat#88-8005-74) was from eBioscience (CA).

The thicknesses of $Ti_3C_2T_x$ and GO were observed via AFM (Icon, Germany) in tapping mode, and the height of the sample was analyzed. Hydrodynamic diameters, dispersity, and ζ-potentials were measured using a dynamic light scattering (DLS) instrument (Zetasizer Nano ZS90, Malvern). The chemical composition and structure of $Ti_3C_2T_x$ were investigated via Raman spectroscopy and XPS. The XRD patterns of $Ti_3C_2T_x$ nanosheets were generated from a Shimazu XRD-6100 X-ray diffractometer (Japan). Raman patterns of $Ti_3C_2T_x$ nanosheets were obtained from a Renishaw inVia laser confocal Raman spectrometer (U.K.). XPS spectra of $Ti_3C_2T_x$ nanosheets were obtained on an X-ray photoelectron spectrometer (EscaLab 250Xi, Thermo Fisher Scientific).

***In Vitro* Hemolysis Assay.** Fresh blood obtained by removing the eyeballs of C57BL/6J mice was collected in an Eppendorf tube prerinsed with heparin and then transferred to a 10 mL centrifuge tube containing 5 mL of physiological saline for mixing before centrifugation at 800 rpm for 5 min to collect RBCs (the supernatant was discarded). All animal experiments were reviewed and approved by the Animal Ethics Committee of Soochow University. The RBCs were washed in physiological saline and further centrifuged until the supernatant turned clear and transparent. The washed RBCs were prepared into a 4% RBC suspension with physiological saline and mixed with an equal volume of $Ti_3C_2T_x$ or GO at different concentrations to obtain a mixed solution of RBCs and $Ti_3C_2T_x$ or GO at a final concentration of 6.25−200 μg/mL. An RBC suspension treated with physiological saline was used as a negative control, and an RBC suspension treated with ultrapure water was used as a positive control. The RBC suspensions in different groups were placed on a metal bath and incubated at 37 °C and 600 rpm for 3 h. After centrifugation at 1500 rpm for 3 min, the RBC morphology of each group was photographed. In addition, 100 μL of each supernatant was placed into a 96-well microplate to obtain the absorbance at 540 nm using a microplate reader (Bio-Tek Instruments, Synergy NEO) and to analyze and calculate the percentage of hemolysis. The percentage of hemolysis was calculated as follows

$$\text{percent hemolysis (\%)} = \left(\frac{(\text{sample abs 540 nm} - \text{negative control abs 540 nm})}{(\text{positive control abs 540 nm} - \text{negative control abs 540 nm})}\right) \times 100 \quad (1)$$

RBC Morphology Observed under Light Microscopy. The RBC pellet in each group after centrifugation in the above experiment was collected and resuspended in 1 mL of normal saline. The resuspended RBCs (10 μL) were dropped onto a glass slide (24 × 64 mm^2) and covered with a glass coverslip (24 × 32 mm^2) for morphological observation and photographing under a light microscope (Olympus, Tokyo, Japan).

RBC Morphology Observed under SEM. The RBC pellet in each group after centrifugation in the above experiment was collected and resuspended in 1 mL of 2.5% glutaraldehyde to fix the cells overnight at 4 °C. After washing the cells in ultrapure water three times (5 min) the next day, the cells were dehydrated through a series of ethanol solutions (30, 50, 70, 80, 90, 95, and 100%) for 10 min each. After dehydration, the RBCs were resuspended in 1 mL of *tert*-butanol, frozen at −20 °C for 20 min and then placed in a freeze dryer. The morphology of RBCs was observed under an SEM (Quanta 200FEG, FEI).

CKK-8 Viability Assay. The HUVECs in the logarithmic growth phase were trypsinized and plated at 5 × 10^3 cells per well in 96-well plates and cultured in complete DMEM containing 10% FBS. The edges of the 96-well plates were sealed with sterile PBS. After 24 h incubation, HUVECs reached ∼80% confluence. Subsequently, HUVECs were incubated with different concentrations of $Ti_3C_2T_x$ or GO (25, 50, 100, and 200 μg/mL) in serum-free DMEM for 24 or 48 h, and then, the cells were washed three times using PBS. The CCK-8 assay was performed according to the manufacturer's instructions. A microplate reader (Bio-Tek Instruments, Synergy NEO) was used to obtain the absorbance (optical density, OD) of

https://doi.org/10.1021/acs.chemrestox.2c00154
Chem. Res. Toxicol. 2023, 36, 347−359

cells in different groups at 450 nm to calculate the viability according to the following equation

$$\text{cell viability} = \left(\frac{OD_{test} - OD_{blank}}{OD_{control} - OD_{blank}}\right) \times 100 \quad (2)$$

where OD_{test} refers to the absorbance of the cells exposed to the nanomaterial sample, $OD_{control}$ refers to the absorbance of the control sample, and OD_{blank} refers to the absorbance of the blank well. Each sample was tested in six replicates.

Live/Dead Assay. The HUVECs were plated at a density of 5×10^3 cells per well in six-well plates and cultured in complete DMEM containing 10% FBS. When confluence reached ∼80%, the HUVECs were incubated with $Ti_3C_2T_x$ or GO (50, 200 μg/mL) in serum-free DMEM. $Ti_3C_2T_x$ and GO samples were dispersed into the concentration of 1000 μg/mL with sterile water and ultrasonicated for 30 min before use. All samples were diluted to concentrations of 25, 50, 100, and 200 μg/mL using FBS-free DMEM before adding them to the cell culture. After being incubated for 24 or 48 h, the medium was aspirated and replaced with fresh medium containing calcein-AM and ethidium homodimer-1 at a concentration of 1 μg·mL^{-1} and placed in a humidified incubator at 37 °C and 5% CO_2 for 30 min. Images were taken by fluorescence microscopy (Leica DMi8, Germany). Approximately 300 cells were counted in both live and dead images. Live/dead experiments were performed as three independent exposures for each treatment medium.

Apoptosis Assay. HUVECs were seeded in six-well plates and cultured under the same condition as the live/dead assay. After being incubated with $Ti_3C_2T_x$ or GO (50, 200 μg/mL) for 48 h, the cells were washed with PBS and added with Annexin V-FITC/PI following the protocol. Apoptosis was analyzed by flow cytometry (BD FACS Verse). The apoptosis ratio was analyzed by Flowjo V10 software.

Assay of Intracellular ROS. The intracellular ROS level was detected by the oxidant-sensitive fluorescent dye 2′,7′-dichlorofluorescin diacetate. DCFH-DA as a nonfluorescent compound can be freely taken up by cells and oxidized to its fluorescent form (2′,7′-dichlorofluorescin, DCF), thereby indicating the level of intracellular ROS. In this study, the HUVECs were exposed to $Ti_3C_2T_x$ or GO nanosheets (50, 200 μg/mL) in serum-free DMEM for 48 h, stained with DCFH-DA following the protocol with the kit, and then analyzed with flow cytometry (BD, FACS Verse). For the fluorescence imaging of DCF and Hoechst 33342, images were captured under a fluorescence microscope (Leica, DMi8, Germany).

MMP Detection. Changes in the mitochondrial membrane potential elicited by $Ti_3C_2T_x$/GO nanosheets were detected using a JC-1 kit, which was processed following the protocol. In brief, HUVECs were seeded in six-well plates and cultured under the same condition as the live/dead assay. After being exposed to $Ti_3C_2T_x$/GO nanosheets for 48 h, the HUVECs were stained with the JC-1 reagent for 20 min and washed with JC-1 buffer (1×). The cells were then imaged using a fluorescence microscope and imaging system (Leica, DMi8, Germany).

Statistical Analysis. Data are presented as the means ± standard deviation (SD) of three parallel experiments. Statistical analysis software SPSS 24.0 (SPSS Inc., Chicago, IL) was used to perform Student's *t*-test. Significance was considered at $^*p < 0.05$, $^{**}p < 0.01$, and $^{***}p < 0.001$.

MD Simulations. MD simulations were performed to study the interface behavior and the underlying mechanisms between $Ti_3C_2T_x$/GO nanosheets and cell membranes. MD simulation is a powerful theoretical method, which has been widely and successfully applied in various investigations on the nano−biomolecules interface interactions. Here, the RBC membrane was molded with 1-palmitoyl-2-oleoyl-sn-glycero-3-phosphocholine (POPC) because the population of phospholipids with phosphocholine head groups is higher than 85% in the entire molar lipid content on the outer membrane leaflet of RBCs.

The size of the model $Ti_3C_2T_x$/GO nanosheet was 5.0 nm × 4.7 nm/5.0 nm × 4.8 nm, respectively. The model and force field parameters of $Ti_3C_2T_x$ were obtained from a previous study.[89] In the GO nanosheet, the mole ratio of epoxy/oxhydryl/carboxyl was 2:2:1. The force field parameters of the GO nanosheet were also taken from a previous literature study.[69] The POPC membrane containing 214 lipids has a lateral size of 7.87 × 7.87 nm^2. The complex of each system was dissolved in a water box (7.87 nm × 7.87 nm × 16.0 nm). To mimic the physiological environment, 0.15 M NaCl (including 90 Na^+ and 90 Cl^-) was added to the system. All MD simulations were performed with the software package GROMACS (version 2019).[90] VMD software (version 1.9.3)[91,92] was adopted to visualize the simulation results. The CHARMM36[93,94] force field and TIP3P[95] water model were adopted for POPC molecules and water molecules, respectively. The *v*-rescale thermostat method was adopted to maintain the simulation temperature at 300 K.[96] The pressure was coupled at 1 atm by the semi-isotropic Parrinello−Rahman barostat method.[97] The periodic boundary condition was applied to all systems. The particle mesh Ewald method was used to calculate the long-range electrostatic interactions.[98] The vdW interactions were treated with a cutoff distance of 1.2 nm. All valence solute bonds were maintained constant at their equilibrium values with the LINCS algorithm.[99] Each system was first energy-minimized using the steepest descent minimization algorithm and pre-equilibrated for 10 ns with restraints applied to the nanosheet positions of the nanosheets. Afterward, 300 ns of data-production simulations were conducted in the isothermal−isobaric (NPT) ensemble. The timestep was set to 2.0 fs, and simulation data were collected every 1 ps.

■ ASSOCIATED CONTENT

Supporting Information

The Supporting Information is available free of charge at https://pubs.acs.org/doi/10.1021/acs.chemrestox.2c00154.

XRD spectrum of $Ti_3C_2T_x$ nanosheets; Raman spectrum of $Ti_3C_2T_x$ nanosheets; XPS spectrum of $Ti_3C_2T_x$ nanosheets; AFM images of GO and $Ti_3C_2T_x$ nanosheets; cell viability of HUVECs at high concentration of two nanosheets; cellular uptake of $Ti_3C_2T_x$ and GO nanosheets in HUVECs; cell membrane adhesion of two nanosheets; impurity analysis of GO nanosheets; hydrodynamic diameters, dispersity, and ζ-potentials of two nanosheets (PDF)

■ AUTHOR INFORMATION

Corresponding Authors

Xiuhua Yin − *State Key Laboratory of Radiation Medicine and Protection, School for Radiological and Interdisciplinary Sciences (RAD-X), Collaborative Innovation Center of Radiation Medicine of Jiangsu Higher Education Institutions, Soochow University, Suzhou 215123, China*; Email: xhyin@suda.edu.cn

Gang Yu − *Department of Data and Information, The Children's Hospital Zhejiang University School of Medicine, Hangzhou 310052, China; Sino-Finland Joint AI Laboratory for Child Health of Zhejiang Province, Hangzhou 310052, China; National Clinical Research Center for Child Health, Hangzhou 310052, China; Polytechnic Institute, Zhejiang University, Hangzhou 310052, China*; orcid.org/0000-0001-9935-9969; Email: yugbme@zju.edu.cn

Authors

Jian Huang − *Department of Data and Information, The Children's Hospital Zhejiang University School of Medicine, Hangzhou 310052, China; Sino-Finland Joint AI Laboratory for Child Health of Zhejiang Province, Hangzhou 310052, China; National Clinical Research Center for Child Health, Hangzhou 310052, China*; orcid.org/0000-0002-1955-4316

Juan Su − *State Key Laboratory of Radiation Medicine and Protection, School for Radiological and Interdisciplinary Sciences (RAD-X), Collaborative Innovation Center of Radiation Medicine of Jiangsu Higher Education Institutions, Soochow University, Suzhou 215123, China*

Zhenyu Hou − *State Key Laboratory of Radiation Medicine and Protection, School for Radiological and Interdisciplinary Sciences (RAD-X), Collaborative Innovation Center of Radiation Medicine of Jiangsu Higher Education Institutions, Soochow University, Suzhou 215123, China*

Jing Li − *Department of Data and Information, The Children's Hospital Zhejiang University School of Medicine, Hangzhou 310052, China; Sino-Finland Joint AI Laboratory for Child Health of Zhejiang Province, Hangzhou 310052, China; National Clinical Research Center for Child Health, Hangzhou 310052, China*

Zheming Li − *Department of Data and Information, The Children's Hospital Zhejiang University School of Medicine, Hangzhou 310052, China; Sino-Finland Joint AI Laboratory for Child Health of Zhejiang Province, Hangzhou 310052, China; National Clinical Research Center for Child Health, Hangzhou 310052, China*

Zhu Zhu − *Department of Data and Information, The Children's Hospital Zhejiang University School of Medicine, Hangzhou 310052, China; Sino-Finland Joint AI Laboratory for Child Health of Zhejiang Province, Hangzhou 310052, China; National Clinical Research Center for Child Health, Hangzhou 310052, China*

Shengtang Liu − *State Key Laboratory of Radiation Medicine and Protection, School for Radiological and Interdisciplinary Sciences (RAD-X), Collaborative Innovation Center of Radiation Medicine of Jiangsu Higher Education Institutions, Soochow University, Suzhou 215123, China*

Zaixing Yang − *State Key Laboratory of Radiation Medicine and Protection, School for Radiological and Interdisciplinary Sciences (RAD-X), Collaborative Innovation Center of Radiation Medicine of Jiangsu Higher Education Institutions, Soochow University, Suzhou 215123, China;* orcid.org/0000-0003-3521-6867

Complete contact information is available at: https://pubs.acs.org/10.1021/acs.chemrestox.2c00154

Author Contributions

[#]J.H. and J.S. contributed equally. G.Y. and X.Y. conceived the concept and designed the study. J.H. and J.S. carried out the characterization of the $Ti_3C_2T_x$ and GO nanosheets. J.H., J.S., J.L., and Z.L. performed cellular experiments. Z.H. and S.L. executed MD simulations. J.H., J.S., X.Y., Z.Y., and G.Y. co-wrote the paper. All authors discussed the results and commented on the manuscript.

Notes

The authors declare no competing financial interest.

■ ACKNOWLEDGMENTS

This work was partially supported by the National Key R&D Program of China (grant number 2019YFE0126200) and National Natural Science Foundation of China (grant numbers 62076218, 22106114, and 22176137).

■ REFERENCES

(1) Naguib, M.; Kurtoglu, M.; Presser, V.; Lu, J.; Niu, J.; Heon, M.; Hultman, L.; Gogotsi, Y.; Barsoum, M. W. Two-dimensional nanocrystals produced by exfoliation of Ti_3AlC_2. *Adv. Mater.* **2011**, *23*, 4248−4253.

(2) Gao, X.-T.; Xie, Y.; Zhu, X.; Sun, K.; Xie, X.; Liu, Y.; Yu, J.; Ding, B. Ultrathin MXene nanosheets decorated with TiO_2 quantum dots as an efficient sulfur host toward fast and stable Li−S batteries. *Small* **2018**, *14*, No. 1802443.

(3) Seh, Z. W.; Fredrickson, K. D.; Anasori, B.; Kibsgaard, J.; Strickler, A. L.; Lukatskaya, M. R.; Gogotsi, Y.; Jaramillo, T. F.; Vojvodic, A. Two-dimensional molybdenum carbide (MXene) as an efficient electrocatalyst for hydrogen evolution. *ACS Energy Lett.* **2016**, *1*, 589−594.

(4) Anasori, B.; Lukatskaya, M. R.; Gogotsi, Y. 2D metal carbides and nitrides (MXenes) for energy storage. *Nat. Rev. Mater.* **2017**, *2*, 16098.

(5) Xiong, D.; Li, X.; Bai, Z.; Lu, S. Recent advances in layered $Ti_3C_2T_X$ MXene for electrochemical energy storage. *Small* **2018**, *14*, No. 1703419.

(6) Pang, J.; Mendes, R. G.; Bachmatiuk, A.; Zhao, L.; Ta, H. Q.; Gemming, T.; Liu, H.; Liu, Z.; Rummeli, M. H. Applications of 2D MXenes in energy conversion and storage systems. *Chem. Soc. Rev.* **2019**, *48*, 72−133.

(7) Zhang, C. J.; Anasori, B.; Seral Ascaso, A.; Park, S. H.; McEvoy, N.; Shmeliov, A.; Duesberg, G. S.; Coleman, J. N.; Gogotsi, Y.; Nicolosi, V. Transparent, flexible, and conductive 2D titanium carbide (MXene) films with high volumetric capacitance. *Adv. Mater.* **2017**, *29*, No. 1702678.

(8) Li, N.; Peng, J.; Ong, W. J.; Ma, T.; Arramel; Zhang, P.; Jiang, J.; Yuan, X.; Zhang, C. MXenes: an emerging platform for wearable electronics and looking beyond. *Matter* **2021**, *4*, 377−407.

(9) Zhang, J.; Kong, N.; Uzun, S.; Levitt, A.; Seyedin, S.; Lynch, P. A.; Qin, S.; Han, M.; Yang, W.; Liu, J.; Wang, X.; Gogotsi, Y.; Razal, J. M. Scalable manufacturing of free-standing, strong $Ti_3C_2T_x$ MXene films with outstanding conductivity. *Adv. Mater.* **2020**, *32*, No. 2001093.

(10) Sarycheva, A.; Polemi, A.; Liu, Y.; Dandekar, K.; Anasori, B.; Gogotsi, Y. 2D titanium carbide (MXene) for wireless communication. *Sci. Adv.* **2018**, *4*, No. eaau0920.

(11) Li, Y.; Tian, X.; Gao, S.; Jing, L.; Li, K.; Yang, H.; Fu, F.; Lee, J. Y.; Guo, Y.; Ho, J. S.; Chen, P. Reversible crumpling of 2D titanium carbide (MXene) nanocoatings for stretchable electromagnetic shielding and wearable wireless communication. *Adv. Funct. Mater.* **2020**, *30*, No. 1907451.

(12) Yun, T.; Kim, H.; Iqbal, A.; Cho, Y. S.; Lee, G. S.; Kim, M. K.; Kim, S. J.; Kim, D.; Gogotsi, Y.; Kim, S. O.; Koo, C. M. Electromagnetic shielding of monolayer MXene assemblies. *Adv. Mater.* **2020**, *32*, No. 1906769.

(13) Iqbal, A.; Sambyal, P.; Koo, C. M. 2D MXenes for electromagnetic shielding: a review. *Adv. Funct. Mater.* **2020**, *30*, No. 2000883.

(14) Shahzad, F.; Alhabeb, M.; Hatter, C. B.; Anasori, B.; Man Hong, S.; Koo, C. M.; Gogotsi, Y. Electromagnetic interference shielding with 2D transition metal carbides (MXenes). *Science* **2016**, *353*, 1137−1140.

(15) Liu, J.; Zhang, H.; Sun, R.; Liu, Y.; Liu, Z.; Zhou, A.; Yu, Z. Hydrophobic, flexible, and lightweight MXene foams for high-performance electromagnetic-interference shielding. *Adv. Mater.* **2017**, *29*, No. 1702367.

(16) Ihsanullah, I. MXenes (two-dimensional metal carbides) as emerging nanomaterials for water purification: Progress, challenges and prospects. *Chem. Eng. J.* **2020**, *388*, No. 124340.

(17) Rasool, K.; Pandey, R. P.; Rasheed, P. A.; Buczek, S.; Gogotsi, Y.; Mahmoud, K. A. Water treatment and environmental remediation applications of two-dimensional metal carbides (MXenes). *Mater. Today* **2019**, *30*, 80−102.

(18) Fei, J.; Koh, S. W.; Tu, W.; Ge, J.; Rezaeyan, H.; Hou, S.; Duan, H.; Lam, Y. C.; Li, H. Functionalized MXene enabled sustainable water harvesting and desalination. *Adv. Sustainable Syst.* **2020**, *4*, No. 2000102.

(19) Chen, J.; Huang, Q.; Huang, H.; Mao, L.; Liu, M.; Zhang, X.; Wei, Y. Recent progress and advances in the environmental applications of MXene related materials. *Nanoscale* **2020**, *12*, 3574−3592.
(20) Huang, K.; Li, Z.; Lin, J.; Han, G.; Huang, P. Two-dimensional transition metal carbides and nitrides (MXenes) for biomedical applications. *Chem. Soc. Rev.* **2018**, *47*, 5109−5124.
(21) Wang, K.; Lou, Z.; Wang, L.; Zhao, L.; Zhao, S.; Wang, D.; Han, W.; Jiang, K.; Shen, G. Bioinspired interlocked structure-induced high deformability for two-dimensional titanium carbide (MXene)/natural microcapsule-based flexible pressure sensors. *ACS Nano* **2019**, *13*, 9139−9147.
(22) Pei, Y.; Zhang, X.; Hui, Z.; Zhou, J.; Huang, X.; Sun, G.; Huang, W. $Ti_3C_2T_X$ MXene for sensing applications: recent progress, design principles, and future perspectives. *ACS Nano* **2021**, *15*, 3996−4017.
(23) Sinha, A.; Zhao, H.; Huang, Y.; Lu, X.; Chen, J.; Jain, R. MXene: An emerging material for sensing and biosensing. *TrAC, Trends Anal. Chem.* **2018**, *105*, 424−435.
(24) Wu, L.; Lu, X.; Wu, Z.; Dong, Y.; Wang, X.; Zheng, S.; Chen, J.; et al. 2D transition metal carbide MXene as a robust biosensing platform for enzyme immobilization and ultrasensitive detection of phenol. *Biosens. Bioelectron.* **2018**, *107*, 69−75.
(25) Wu, L.; You, Q.; Shan, Y.; Gan, S.; Zhao, Y.; Dai, X.; Xiang, Y. Few-layer $Ti_3C_2T_x$ MXene: A promising surface plasmon resonance biosensing material to enhance the sensitivity. *Sens. Actuators, B* **2018**, *277*, 210−215.
(26) Liu, J.; Jiang, X.; Zhang, R.; Zhang, Y.; Wu, L.; Lu, W.; Li, J.; Li, Y.; Zhang, H. MXene-enabled electrochemical microfluidic biosensor: applications toward multicomponent continuous monitoring in whole blood. *Adv. Funct. Mater.* **2019**, *29*, No. 1807326.
(27) Chao, M.; He, L.; Gong, M.; Li, N.; Li, X.; Peng, L.; Shi, F.; Zhang, L.; Wan, P. Breathable $Ti_3C_2T_x$ MXene/protein nanocomposites for ultrasensitive medical pressure sensor with degradability in solvents. *ACS Nano* **2021**, *15*, 9746−9758.
(28) Rasool, K.; Mahmoud, K. A.; Johnson, D. J.; Helal, M.; Berdiyorov, G. R.; Gogotsi, Y. Efficient antibacterial membrane based on two-dimensional $Ti_3C_2T_x$ (MXene) nanosheets. *Sci. Rep.* **2017**, *7*, No. 1598.
(29) Rasool, K.; Helal, M.; Ali, A.; Ren, C. E.; Gogotsi, Y.; Mahmoud, K. A. Antibacterial activity of $Ti_3C_2T_x$ MXene. *ACS Nano* **2016**, *10*, 3674−3684.
(30) Shamsabadi, A. A.; Sharifian, G. M.; Anasori, B.; Soroush, M. Antimicrobial mode-of-action of colloidal $Ti_3C_2T_x$ MXene nanosheets. *ACS Sustainable Chem. Eng.* **2018**, *6*, 16586−16596.
(31) Liu, Y.; Tian, Y.; Han, Q.; Yin, J.; Zhang, J.; Yu, Y.; Yang, W.; Deng, Y. Synergism of 2D/1D MXene/cobalt nanowire heterojunctions for boosted photo-activated antibacterial application. *Chem. Eng. J.* **2021**, *410*, No. 128209.
(32) Zhou, L.; Zheng, H.; Liu, Z.; Wang, S.; Liu, Z.; Chen, F.; Zhang, H.; Kong, J.; Zhou, F.; Zhang, Q. Conductive antibacterial hemostatic multifunctional scaffolds based on $Ti_3C_2T_x$ MXene nanosheets for promoting multidrug-resistant bacteria-infected wound healing. *ACS Nano* **2021**, *15*, 2468−2480.
(33) Han, X.; Huang, J.; Lin, H.; Wang, Z.; Li, P.; Chen, Y. 2D ultrathin MXene-based drug-delivery nanoplatform for synergistic photothermal ablation and chemotherapy of cancer. *Adv. Healthcare Mater.* **2018**, *7*, No. 1701394.
(34) Liu, Y.; Han, Q.; Yang, W.; Gan, X.; Yang, Y.; Xie, K.; Xie, L.; Deng, Y. Two-dimensional MXene/cobalt nanowire heterojunction for controlled drug delivery and chemo-photothermal therapy. *Mater. Sci. Eng. C* **2020**, *116*, No. 111212.
(35) Li, Z.; Zhang, H.; Han, J.; Chen, Y.; Lin, H.; Yang, T. Surface nanopore engineering of 2D MXenes for targeted and synergistic multitherapies of hepatocellular carcinoma. *Adv. Mater.* **2018**, *30*, No. 1706981.
(36) Yu, X.; Cai, X.; Cui, H.; Lee, S. W.; Yu, X. F.; Liu, B. Fluorine-free preparation of titanium carbide MXene quantum dots with high near-infrared photothermal performances for cancer therapy. *Nanoscale* **2017**, *9*, 17859−17864.
(37) Liang, R.; Li, Y.; Huo, M.; Lin, H.; Chen, Y. Triggering sequential catalytic fenton reaction on 2D MXenes for hyperthermia-augmented synergistic nanocatalytic cancer therapy. *ACS Appl. Mater. Interfaces* **2019**, *11*, 42917−42931.
(38) Li, R.; Zhang, L.; Shi, L.; Wang, P. MXene Ti_3C_2: an effective 2D light-to-heat conversion material. *ACS Nano* **2017**, *11*, 3752−3759.
(39) Lin, H.; Wang, X.; Yu, L.; Chen, Y.; Shi, J. Two-dimensional ultrathin MXene ceramic nanosheets for photothermal conversion. *Nano Lett.* **2017**, *17*, 384−391.
(40) Lin, H.; Gao, S.; Dai, C.; Chen, Y.; Shi, J. A two-dimensional biodegradable niobium carbide (MXene) for photothermal tumor eradication in NIR-I and NIR-II biowindows. *J. Am. Chem. Soc.* **2017**, *139*, 16235−16247.
(41) Yan, X.; Wang, K.; Zhao, J.; Zhou, Z.; Wang, H.; Wang, J.; Zhang, L.; Li, X.; Xiao, Z.; Zhao, Q.; et al. A new memristor with 2D $Ti_3C_2T_x$ MXene flakes as an artificial bio-synapse. *Small* **2019**, *15*, No. 1900107.
(42) Sokolov, A.; Ali, M.; Li, H.; Jeon, Y. R.; Ko, M. J.; Choi, C. Partially oxidized MXene $Ti_3C_2T_x$ sheets for memristor having synapse and threshold resistive switching characteristics. *Adv. Electron. Mater.* **2021**, *7*, No. 2000866.
(43) Xue, Q.; Zhang, H.; Zhu, M.; Pei, Z.; Li, H.; Wang, Z.; Huang, Y.; Huang, Y.; Deng, Q.; Zhou, J.; et al. Photoluminescent Ti_3C_2 MXene quantum dots for multicolor cellular imaging. *Adv. Mater.* **2017**, *29*, No. 1604847.
(44) Wang, Z.; Xuan, J.; Zhao, Z.; Li, Q.; Geng, F. Versatile cutting method for producing fluorescent ultrasmall MXene sheets. *ACS Nano* **2017**, *11*, 11559−11565.
(45) Guan, Q.; Ma, J.; Yang, W.; Zhang, R.; Zhang, X.; Dong, X.; Fan, Y.; Cai, L.; Cao, Y.; Zhang, Y.; et al. Highly fluorescent Ti_3C_2 MXene quantum dots for macrophage labeling and Cu^{2+} ion sensing. *Nanoscale* **2019**, *11*, 14123−14133.
(46) Jin, L.; Guo, X.; Gao, D.; Wu, C.; Hu, B.; Tan, G.; Du, N.; Cai, X.; Yang, Z.; Zhang, X. NIR-responsive MXene nanobelts for wound healing. *NPG Asia Mater.* **2021**, *13*, 24.
(47) Ahamed, M.; Akhtar, M. J.; Khan, M. A. M.; Karuppiah, P. Antibacterial, antifungal, and anticancer potential of two-dimensional $Ti_3C_2T_x$ MXene. *Mater. Lett.* **2022**, *327*, No. 133020.
(48) Xuan, J.; Wang, Z.; Chen, Y.; Liang, D.; Cheng, L.; Yang, X.; Liu, Z.; Ma, R.; Sasaki, T.; Geng, F. Organic-base-driven intercalation and delamination for the production of functionalized titanium carbide nanosheets with superior photothermal therapeutic performance. *Angew. Chem.* **2016**, *128*, 14789−14794.
(49) Liu, G.; Zou, J.; Tang, Q.; Yang, X.; Zhang, Y.; Zhang, Q.; Huang, W.; Chen, P.; Shao, J.; Dong, X. Surface modified Ti_3C_2 MXene nanosheets for tumor targeting photothermal/photodynamic/chemo synergistic therapy. *ACS Appl. Mater. Interfaces* **2017**, *9*, 40077−40086.
(50) Dai, C.; Lin, H.; Xu, G.; Liu, Z.; Wu, R.; Chen, Y. Biocompatible 2D titanium carbide (MXenes) composite nanosheets for pH-responsive MRI-guided tumor hyperthermia. *Chem. Mater.* **2017**, *29*, 8637−8652.
(51) Han, X.; Jing, X.; Yang, D.; Lin, H.; Wang, Z.; Ran, H.; Li, P.; Chen, Y. Therapeutic mesopore construction on 2D Nb_2C MXenes for targeted and enhanced chemo-photothermal cancer therapy in NIR-II biowindow. *Theranostics* **2018**, *8*, 4491.
(52) Liu, Z.; Lin, H.; Zhao, M.; Dai, C.; Zhang, S.; Peng, W.; Chen, Y. 2D superparamagnetic tantalum carbide composite MXenes for efficient breast-cancer theranostics. *Theranostics* **2018**, *8*, 1648−1664.
(53) Lin, H.; Wang, Y.; Gao, S.; Chen, Y.; Shi, J. Theranostic 2D tantalum carbide (MXene). *Adv. Mater.* **2018**, *30*, No. 1703284.
(54) Szuplewska, A.; Kulpińska, D.; Dybko, A.; Jastrzębska, A. M.; Wojciechowski, T.; Rozmysłowska, A.; Chudy, M.; Grabowska-Jadach, I.; Ziemkowska, W.; Brzózka, Z.; Olszyna, A. 2D Ti_2C (MXene) as a novel highly efficient and selective agent for photothermal therapy. *Mater. Sci. Eng. C* **2019**, *98*, 874−886.

https://doi.org/10.1021/acs.chemrestox.2c00154
Chem. Res. Toxicol. 2023, 36, 347−359

(55) Lim, G. P.; Soon, C. F.; Ma, N. L.; Morsin, M.; Nayan, N.; Ahmad, M. K.; Tee, K. S. Cytotoxicity of MXene-based nanomaterials for biomedical applications: A mini review. *Environ. Res.* **2021**, *201*, No. 111592.
(56) Wu, J.; Yu, Y.; Su, G. Safety assessment of 2D MXenes: in vitro and in vivo. *Nanomaterials* **2022**, *12*, 828.
(57) Iravani, S.; Varma, R. S. MXenes for cancer therapy and diagnosis: recent advances and current challenges. *ACS Biomater. Sci. Eng.* **2021**, *7*, 1900−1913.
(58) Zhang, D.; Zheng, W.; Li, X.; Li, A.; Ye, N.; Zhang, L.; Liu, Y.; Liu, X.; Zhang, R.; Wang, M.; Cheng, J.; Yang, H.; Gong, M. Investigating the effect of Ti_3C_2 (MXene) nanosheet on human umbilical vein endothelial cells via a combined untargeted and targeted metabolomics approach. *Carbon* **2021**, *178*, 810−821.
(59) Gu, M.; Dai, Z.; Yan, X.; Ma, J.; Niu, Y.; Lan, W.; Wang, X.; Xu, Q. Comparison of toxicity of Ti_3C_2 and Nb_2C Mxene quantum dots (QDs) to human umbilical vein endothelial cells. *J. Appl. Toxicol.* **2021**, *41*, 745−754.
(60) Jastrzębska, A.; Szuplewska, A.; Wojciechowski, T.; Chudy, M.; Ziemkowska, W.; Chlubny, L.; Rozmysłowska, A.; Olszyna, A. In vitro studies on cytotoxicity of delaminated Ti_3C_2 MXene. *J. Hazard. Mater.* **2017**, *339*, 1−8.
(61) Scheibe, B.; Wychowaniec, J. K.; Scheibe, M.; Peplińska, B.; Jarek, M.; Nowaczyk, G.; Przysiecka, Ł. Cytotoxicity assessment of Ti−Al−C based MAX phases and $Ti_3C_2T_x$ MXenes on human fibroblasts and cervical cancer cells. *ACS Biomater. Sci. Eng.* **2019**, *5*, 6557−6569.
(62) Wu, W.; Ge, H.; Zhang, L.; Lei, X.; Yang, Y.; Fu, Y.; Feng, H. Evaluating the cytotoxicity of Ti_3C_2 MXene to neural stem cells. *Chem. Res. Toxicol.* **2020**, *33*, 2953−2962.
(63) Jang, J. H.; Lee, E. J. Influence of MXene particles with a stacked-lamellar structure on osteogenic differentiation of human mesenchymal stem cells. *Materials* **2021**, *14*, 4453.
(64) Parhiz, H.; Khoshnejad, M.; Myerson, J. W.; Hood, E.; Patel, P. N.; Brenner, J. S.; Muzykantov, V. R. Unintended effects of drug carriers: big issues of small particles. *Adv. Drug Delivery Rev.* **2018**, *130*, 90−112.
(65) Guo, Q.; Yang, Y.; Zhao, L.; Chen, J.; Duan, G.; Yang, Z.; Zhou, R. Graphene oxide toxicity in W^{1118} flies. *Sci. Total Environ.* **2022**, *805*, No. 150302.
(66) Liao, K. H.; Lin, Y. S.; Macosko, C. W.; Haynes, C. L. Cytotoxicity of graphene oxide and graphene in human erythrocytes and skin fibroblasts. *ACS Appl. Mater. Interfaces* **2011**, *3*, 2607−2615.
(67) Liu, L.; Zhang, S.; Zhao, L.; Gu, Z.; Duan, G.; Zhou, B.; Yang, Z.; Zhou, R. Superior compatibility of C_2N with human red blood cell membranes and the underlying mechanism. *Small* **2018**, *14*, No. 1803509.
(68) Dobrovolskaia, M. A.; Clogston, J. D.; Neun, B. W.; Hall, J. B.; Patri, A. K.; McNeil, S. E. Method for analysis of nanoparticle hemolytic properties in vitro. *Nano Lett.* **2008**, *8*, 2180−2187.
(69) Tu, Y. S.; Lv, M.; Xiu, P.; Huynh, T.; Zhang, M.; Castelli, M.; Liu, Z. R.; Huang, Q.; Fan, C. H.; Fang, H. P.; Zhou, R. H. Destructive extraction of phospholipids from Escherichia coli membranes by graphene nanosheets. *Nat. Nanotechnol.* **2013**, *8*, 594−601.
(70) Duan, G.; Kang, S.-g.; Tian, X.; Garate, J. A.; Zhao, L.; Ge, C.; Zhou, R. Protein corona mitigates the cytotoxicity of graphene oxide by reducing its physical interaction with cell membrane. *Nanoscale* **2015**, *7*, 15214−15224.
(71) Li, Y.; Yuan, H.; von Dem Bussche, A.; Creighton, M.; Hurt, R. H.; Kane, A. B.; Gao, H. Graphene microsheets enter cells through spontaneous membrane penetration at edge asperities and corner sites. *Proc. Natl. Acad. Sci. U.S.A.* **2013**, *110*, 12295−12300.
(72) Lotfi, R.; Naguib, M.; Yilmaz, D. E.; Nanda, J.; van Duin, A. C. T. A comparative study on the oxidation of two-dimensional Ti_3C_2 MXene structures in different environments. *J. Mater. Chem. A* **2018**, *6*, 12733−12743.
(73) Gómez-Navarro, C.; Meyer, J. C.; Sundaram, R. S.; Chuvilin, A.; Kurasch, S.; Burghard, M.; Kern, K.; Kaiser, U. Atomic structure of reduced graphene oxide. *Nano Lett.* **2010**, *10*, 1144−1148.
(74) Erickson, K.; Erni, R.; Lee, Z.; Alem, N.; Gannett, W.; Zettl, A. Determination of the local chemical structure of graphene oxide and reduced graphene oxide. *Adv. Mater.* **2010**, *22*, 4467−4472.
(75) Dave, S. H.; Gong, C.; Robertson, A. W.; Warner, J. H.; Grossman, J. C. Chemistry and structure of graphene oxide via direct imaging. *ACS Nano* **2016**, *10*, 7515−7522.
(76) Yin, X.; Zhang, S.; Wen, L.; Su, J.; Huang, J.; Duan, G.; Yang, Z. Nonmonotonic relationship between the oxidation state of graphene-based materials and its cell membrane damage Effects. *ACS Appl. Mater. Interfaces* **2022**, *14*, 30306−30314.
(77) Yang, Y.; Han, P.; Xie, X.; Yin, X.; Duan, G.; Wen, L. Protein corona reduced graphene oxide cytotoxicity by inhibiting endocytosis. *Colloids Interface Sci. Commun.* **2021**, *45*, No. 100514.
(78) Liu, S.; Xu, A.; Gao, Y.; Xie, Y.; Liu, Z.; Sun, M.; Mao, H.; Wang, X. Graphene oxide exacerbates dextran sodium sulfate-induced colitis via ROS/AMPK/p53 signaling to mediate apoptosis. *J. Nanobiotechnol.* **2021**, *19*, 85.
(79) Birch-Machin, M. A.; Turnbull, D. M. Assaying mitochondrial respiratory complex activity in mitochondria isolated from human cells and tissues. *Methods Cell Biol.* **2001**, *65*, 97−117.
(80) Galluzzi, L.; Zamzami, N.; de La Motte Rouge, T.; Lemaire, C.; Brenner, C.; Kroemer, G. Methods for the assessment of mitochondrial membrane permeabilization in apoptosis. *Apoptosis* **2007**, *12*, 803−813.
(81) Chong, Y.; Ge, C.; Yang, Z.; Garate, J. A.; Gu, Z.; Weber, J. K.; Liu, J.; Zhou, R. Reduced Cytotoxicity of Graphene Nanosheets Mediated by Blood-Protein Coating. *ACS Nano* **2015**, *9*, 5713−5724.
(82) Zhao, X.; Vashisth, A.; Prehn, E.; Sun, W.; Shah, S. A.; Habib, T.; Chen, Y.; Tan, Z.; Lutkenhaus, J. L.; Radovic, M.; Green, M. J. Antioxidants unlock shelf-stable $Ti_3C_2T_x$ (MXene) nanosheet dispersions. *Matter* **2019**, *1*, 513−526.
(83) Zhang, C. J.; Pinilla, S.; McEvoy, N.; Cullen, C. P.; Anasori, B.; Long, E.; Park, S.-H.; Seral-Ascaso, A.; Shmeliov, A.; Krishnan, D.; Morant, C.; Liu, X.; Duesberg, G. S.; Gogotsi, Y.; Nicolosi, V. Oxidation stability of colloidal two-dimensional titanium carbides (MXenes). *Chem. Mater.* **2017**, *29*, 4848−4856.
(84) Lipatov, A.; Alhabeb, M.; Lukatskaya, M. R.; Boson, A.; Gogotsi, Y.; Sinitskii, A. Effect of synthesis on quality, electronic properties and environmental stability of individual monolayer Ti_3C_2 MXene flakes. *Adv. Electron. Mater.* **2016**, *2*, No. 1600255.
(85) Mashtalir, O.; Cook, K. M.; Mochalin, V. N.; Crowe, M.; Barsoum, M. W.; Gogotsi, Y. Dye adsorption and decomposition on two-dimensional titanium carbide in aqueous media. *J. Mater. Chem. A* **2014**, *2*, 14334−14338.
(86) Ghassemi, H.; Harlow, W.; Mashtalir, O.; Beidaghi, M.; Lukatskaya, M. R.; Gogotsi, Y.; Taheri, M. L. In situ environmental transmission electron microscopy study of oxidation of two-dimensional Ti_3C_2 and formation of carbon-supported TiO_2. *J. Mater. Chem. A* **2014**, *2*, 14339−14343.
(87) Maleski, K.; Mochalin, V. N.; Gogotsi, Y. Dispersions of two-dimensional titanium carbide MXene in organic solvents. *Chem. Mater.* **2017**, *29*, 1632−1640.
(88) Habib, T.; Zhao, X.; Shah, S. A.; Chen, Y.; Sun, W.; An, H.; Lutkenhaus, J. L.; Radovic, M.; Green, M. J. Oxidation stability of $Ti_3C_2T_x$ MXene nanosheets in solvents and composite films. *npj 2D Mater. Appl.* **2019**, *3*, 8.
(89) Xu, K.; Ji, X.; Zhang, B.; Chen, C.; Ruan, Y.; Miao, L.; Jiang, J. Charging/Discharging Dynamics in Two-Dimensional Titanium Carbide (MXene) Slit Nanopore: Insights from molecular dynamic study. *Electrochim. Acta* **2016**, *196*, 75−83.
(90) Van Der Spoel, D.; Lindahl, E.; Hess, B.; Groenhof, G.; Mark, A. E.; Berendsen, H. J. C. GROMACS: Fast, flexible, and free. *J. Comput. Chem.* **2005**, *26*, 1701−1718.
(91) Humphrey, W.; Dalke, A.; Schulten, K. VMD: Visual molecular dynamics. *J. Mol. Graphics* **1996**, *14*, 33−38.

https://doi.org/10.1021/acs.chemrestox.2c00154
Chem. Res. Toxicol. 2023, 36, 347−359

(92) Wu, C.; Liu, S.; Zhang, S.; Yang, Z. Molcontroller: A VMD Graphical User Interface Featuring Molecule Manipulation. *J. Chem. Inf. Model.* **2020**, *60*, 5126−5131.
(93) Brooks, B. R.; Bruccoleri, R. E.; Olafson, B. D.; States, D. J.; Swaminathan, S.; Karplus, M. Charmm - a Program for Macromolecular Energy, Minimization, and Dynamics Calculations. *J. Comput. Chem.* **1983**, *4*, 187−217.
(94) Klauda, J. B.; Venable, R. M.; Freites, J. A.; O'Connor, J. W.; Tobias, D. J.; Mondragon-Ramirez, C.; Vorobyov, I.; MacKerell, A. D.; Pastor, R. W. Update of the CHARMM All-Atom Additive Force Field for Lipids: Validation on Six Lipid Types. *J. Phys. Chem. B* **2010**, *114*, 7830−7843.
(95) Jorgensen, W. L.; Chandrasekhar, J.; Madura, J. D.; Impey, R. W.; Klein, M. L. Comparison of Simple Potential Functions for Simulating Liquid Water. *J. Chem. Phys.* **1983**, *79*, 926−935.
(96) Bussi, G.; Donadio, D.; Parrinello, M. Canonical sampling through velocity rescaling. *J. Chem. Phys.* **2007**, *126*, No. 014101.
(97) Parrinello, M.; Rahman, A. Polymorphic Transitions in Single-Crystals - a New Molecular-Dynamics Method. *J. Appl. Phys.* **1981**, *52*, 7182−7190.
(98) Darden, T.; York, D.; Pedersen, L. Particle Mesh Ewald - an N.Log(N) Method for Ewald Sums in Large Systems. *J. Chem. Phys.* **1993**, *98*, 10089−10092.
(99) Hess, B.; Bekker, H.; Berendsen, H. J. C.; Fraaije, J. G. E. M. LINCS: A linear constraint solver for molecular simulations. *J. Comput. Chem.* **1997**, *18*, 1463−1472.

https://doi.org/10.1021/acs.chemrestox.2c00154
Chem. Res. Toxicol. 2023, 36, 347−359